J Mater Sci (2016) 51:2499–2511
DOI 10.1007/s10853-015-9562-3

Porous and fractal analysis on the permeability of nanofiltration membranes for the removal of metal ions

Oluranti Agboola[1,2] · Touhami Mokrani[1] · Rotimi Sadiku[2]

Received: 8 August 2015 / Accepted: 2 November 2015 / Published online: 11 November 2015

Abstract Porous and fractal analysis on the permeability of nanofiltration membranes was investigated for the removal of metal ions. The permeability of a porous membranes used in wastewater treatment is strongly depended on its local geometry and connectivity, the size distribution of the pores available for flow. Fouling studies with two different membranes at three different pHs were carried out with manganese and magnesium. It was shown that the tighter membrane was less rougher and less fouled compared with the rougher membrane. NF90-2450 showed the highest degree of fouling. The X-ray diffraction showed that NF90-2540 consist of a pronounced diamond at the angle of 45 °C which was responsible for porosity. The threshold images were obtained from the scanning electron microscopy images with the use of Image J software confirmed that NF90-2540 has higher percentage porosity when compared with the percentage porosity of NF1540-3. An evaluation of the relationships between porosity and permeability for the fractal analysis by a box counting was done. The evaluation also confirmed that the lower fractal dimension corresponds to a lower value of porosity. The higher the pH, the lower the fractal dimension of the used membranes due to the blockage of pores. A higher value of fractal dimension of the used membrane at a lower pH corresponds to a lower rejection of the metal ions.

✉ Oluranti Agboola
funmi2406@gmail.com

[1] Department of Civil and Chemical Engineering, University of South Africa, Johannesburg, South Africa

[2] Department of Chemical, Metallurgical and Materials Engineering, Tshwane University of Technology, Pretoria, South Africa

Introduction

Nanofiltration (NF) membranes separation process is mainly a liquid-phase separation process because it separates a wide range of organic and inorganic substances from solution in liquid. They are porous membranes, and since the pores are on the order of ten angstroms or less, their performance lies between that of reverse osmosis (RO) and ultrafiltration membranes (UF) membranes. The physical and chemical properties of nanofiltration membranes are very significant in order to understand how nanofiltration membrane functions with respect to the membrane performance. Nanofiltration membranes have to possess the physical attributes that gives appropriate interactions with solutes in the process stream for optimum operation. The mechanism of nanofiltration membrane separation process is diffusion and convection through the membrane pores with the aid of pressure differentials. As far as nanofiltration membranes are concerned, retention and permeability are a function of electric charge and the valence of the salts and compounds in the solution.

Permeability is a measure of the flow conductance of a matrix. This conductance describes the hydro-dynamic behavior of flow through the matrix, which is a porous medium [1]. The research and practical application of porous membranes is due to their high rate of permeability for useful applications in wastewater treatment. Porous media permeability have received great attention due to their research and practical applications in oil production, combustion technology, soil science and engineering, polymer composite mold and heat pipes, and chemical engineering [2–7]. Surface porosity is considered a very important parameter, together with pore size distribution and pore shape. With respect to permeability this is only partially true, because the total skin porosity (surface

porosity together with the length of the pore) will determine the membrane resistance. Total skin porosity and surface porosity of a porous medium can deviate to a large extent depending on the structure of the skin [8]. Thus, surface porosity can have a very high impact on flux decline during the actual filtration process because of the structure of the membrane. Since the microstructures of the porous media are usually disordered and extremely complicated, finding the permeability that represents the system using analytical and numerical approaches can be difficult. Understanding the mechanisms for permeability in a porous medium through analytical solution can also be challenging [9]. The study of transport of gases and liquids through the pore space of membranes is a subject of great importance in the development of advanced membrane-based separation processes [10, 11]. It is very important to understand the relationship between the structure and transport properties of porous membranes since morphology-related parameters (pore size, pore size distribution, membrane thickness, and pore shape) contribute to the performance of membranes.

The determination of cake layer permeability is very important in order to have an accurate analysis and design of membrane filtration; thus fractal theory can be used to evaluate the cake layer permeability in nanofiltration of wastewater. Fractal theory is a relatively new theory used in analyzing natural phenomenon, which allows the characterization of objects in terms of their self-similar (scale invariant) properties (i.e., parts of the object are similar to the whole after rescaling) [12]. Fractal techniques have been used in diverse engineering applications that involve physical phenomena in disordered structures and over multiple scales [12–15]. The importance of studying the failure and morphological-textural characteristics of porous structures used for the preparation of porous materials has also been assumed by fractal analysis [13, 16]. Fractal analysis has the potential to quantify the irregularity and complexity of fractures with measurable value that will describe the geometrical features of cracks, surface or textures in the study of materials of labyrinthine nature [17, 18]. The measure of a fractal object, $M(L)$, is related to the length scale, L, following the scaling law in the form of

$$M(L) \sim L^{D_s}. \tag{1}$$

Equation 1 indicates the property of self-similarity; this means that the value calculated from Eq. 1 remains constant over a range of length scales, L. The geometry structures such as Koch curve, Sierpinski gasket, and Sierpinski carpet are the examples of the exact self-similar fractals, which exhibit the self-similarity over an infinite range of length scales [19]. However, self-similarity in a global sense is seldom observed in actual applications. Numerous objects found in nature are not exactly self-similarity, but statistical self-similarity, which implies that these objects exhibit the self-similarity in some average sense and over a certain local range of length scales, L [20]. Cai et al. [21] recently developed a more generalized spontaneous imbibition model by considering the different sizes and shapes of pores, the tortuosity of imbibition streamlines in random porous media, and the initial wetting-phase saturation. The interrelationships of accumulated imbibition weight, imbibition rate, and gas recovery together with the properties of the porous media, wetting liquids, and their interactions were derived analytically. A theoretical analysis and comparison of their results denoted that the equations they presented can generalize several traditional and newly developed models from the literature. The proposed model was evaluated using previously published data for spontaneous imbibition measured in various natural and engineered materials including different rock types, fibrous materials, and silica glass. Their results showed that the generalized model can be used to characterize the spontaneous imbibition behavior of many different porous media and that the pore shape cannot always be assumed to be cylindrical. Some researchers developed a Sierpinski fractal model, which is a useful tool to analysis cake pore area distribution and its permeability [22–24]. The model was described as

$$B(\geq r) = S_c - \int_r^{r_{max}} f(r)\pi r^2 dr = C_0(\pi r^2)^{2-D_s}, \tag{2}$$

where S_c is the total cake layer area analyzed, $f(r)$ is radii distribution function of cake layer pores, r is the size of a pore, r_{max} is the size of the biggest pore, B is the area of the cake layer subtracted all the area of the pores which size larger than r, defined as surplus area, C_0 is a constant, the fractal dimension, D_s, represents the pore area distribution of the cake layer. The calculation procedure of D_s was as follows [20]:

(1) Evaluate each pore area using an image analyser.
(2) Define several different area levels/thresholds, a_i, for all the pores.
(3) Sum all the pores which are equal or larger than ai, and defined as:

$$A_i = \sum_i a_i \tag{3}$$

Based on Eqs. 2 and 3, a new model was developed:

$$B_i(\geq a_1) = S_c - A_i = C_0 a_i^{2-D_s}. \tag{4}$$

A Richardson plot is a plot that shows the relationship between the step length and the perimeter length [25]. Therefore, a Richardson plot of ln B_i versus ln a_i yields a straight line of slope 2-D_s, enabling the fractal dimension,

D_s, of the cake surface to be determined [26]. The fractal dimension (FD) is a characteristic parameter that quantitatively describes the complex degree. The fractal dimension structure of the nanofiltration membranes, has not been explored until now, and is one of the key factor determining membrane permeate flux. Due to the effective nature of fractal dimensions in different structures of membranes (in microfiltration of activated sludge wastewater [20] and in membrane bioreactor [26]), the objective of this study is to investigate the porosity and fractal analysis of nanofiltration membranes permeability. In the present work, a fractal dimension by box-counting method will be use to analyze the flux permeability based on the microstructure of the diffusion layer obtained by SEM. Porosity of the membranes are involved in this analysis.

Experimental

Nanofiltration membrane characteristics

Two composite nanofiltration membranes (NF1540-3 from Bio Pure Technology (BPT), Israel and NF90-2540 from Dow-Filmtec, South Africa) were chosen as representative of a class of thin-film composite membranes which are acid stable in wastewater treatment applications. The two membranes were chosen based on their surface layer of melamine polyamine on a polyethersulfone support with a molecular weight cut off of 400 Da and of 250 Da, respectively. Analytical grade of magnesium sulfate ($MgSO_4$) and manganese sulfate ($MnSO_4$) were used.

Sample preparation

The experiments were conducted with one liter solution containing a magnesium sulfate solution ($MgSO_4$) and manganese sulfate solution ($MnSO_4$) with concentrations of 100 mg L^{-1} each. The salts used were obtained from Associated Chemicals Enterprises Pty Ltd, South Africa and the purity of $MgSO_4$ and $MnSO_4$ is 99 and 98 %, respectively. The solution pH was varied: 2, 3, and 4. The experiments were conducted by using 1000-mL stirring cell membrane filtration apparatus (Memcon, South Africa) equipped with magnetic stirrer. A membrane sheet was fitted to the cell. The membrane active area is about 0.01075 m^2. Operating pressure of 10 bar was employed via high pressure regulator and a nitrogen gas cylinder for NF1540-3 and NF90-2540, respectively. The salts used in preparing the synthetic solutions are analytical grade salts.

Laboratory dead-end test cell

The investigation was done using a Memcon laboratory stirring cell as shown in Fig. 1. The membrane tested was placed in the stirring cell. A liter of sample was then placed in the cell at the product inlet. Pressure was then applied via nitrogen gas and the permeate was collected and its mass determined.

Analytical method

Magnesium and manganese ion concentrations were analyzed by using inductively coupled plasma optical emission. Measurements of the solution pH and temperature were made with a pH meter (Mettler Toledo FG20) and thermometer, respectively.

Analysis of results

Permeate flux and rejections were investigated as function of the working parameters such as operating time and water recovery. The observed rejection, which is the measure of how well a membrane retains a solute, was calculated using Eq. 5

$$\text{Salt Rejection} = (1 - C_P/C_f) \times 100\%, \quad (5)$$

where C_p and C_f are the solution concentrations in the permeate and in the feed solution, respectively.

The permeate flux, J_v (L m^{-2} h^{-1}), was determined by measuring the volume of permeate collected in a given time interval divided with membrane area, using Eq. 6. The flux in this study was considered with respect to the time of filtration; thus transmembrane pressure was constant throughout the filtration experiment and was not taken into account in Eq. 6

$$J_v = V_P/(A \times \Delta t), \quad (6)$$

where V_p is the volume of permeate (L) collected during the sampling time Δt (h) and A is the effective membrane (m^2).

Membrane characterization techniques

Recent progresses in the synthesis and characterization of engineered nanofiltration membranes have brought about new concepts for the design of membranes with increased permeability, selectivity, and resistance to fouling [26–30]. X-ray diffraction (XRD) was used to identify the chemical phase of the membranes. WAXD Pan Analytical Xpert Pro diffractometer, using a CuK_α radiation with a wavelength of 0.15 nm, a voltage of 45 kV, and a current 40 mA was

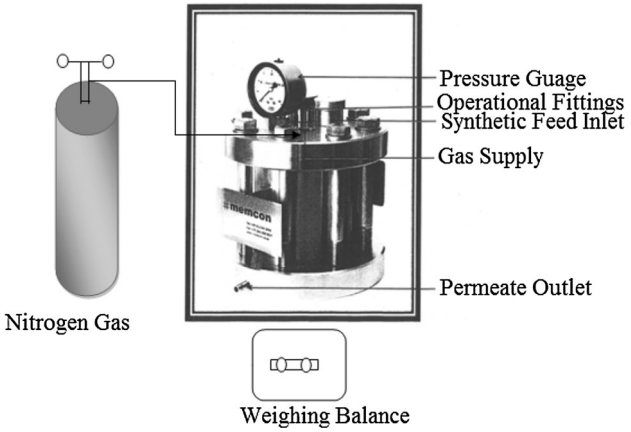

Fig. 1 Schematic diagram of laboratory stirring filtration system; the synthetic feed flow is forced through the membrane at a given pressure through nitrogen gas. The fluid passes through the membrane and all particles larger than the pore sizes of the membrane are retained at its surface

employed for the XRD characterization of the membranes. atomic force microscopy (AFM) was used to characterize the surface roughness. Clean membranes were cut into small pieces and glued onto a sample holder with an agar tape before non-contact AFM imaging was performed using an Agilent Technologies 5500 scanning probe microscope (PicoPlus-Atomic Force Microscopy Series 5500). The AFM cantilever used was made of silicon (Nanosensors) with a resonant frequency of $\sim$60 kHz, a nominal spring constant of 7.4 N m^{-1} with a typical tip radius of less than 7 nm. The AFM measurements were performed on dry membranes in an air atmosphere with relative humidity of $\sim$30 %. The AFM images were flattened with order 1 and the root-mean-squared (rms) value of the roughness was obtained by using the Nanotechnology Research Tool [31]. The scanning electron microscopy (SEM) setup used to visualize the surfaces of the membranes was a Joel Field Emission Electron Microscope JESM-7600F. The virgin membranes were mounted on a double-sided carbon tape and the surfaces were coated with iridium ($\approx$5 nm thickness) to make it conductive. The samples were exposed to an electron beam at an accelerating voltage of 15 kV to obtain a signal for the SEM studies. The micro-marker on the micrographs was used to estimate the pore size (diameter). Clean membrane was cut into small pieces and glued onto a sample holder with an agar tape before non-contact AFM imaging was performed using Agilent Technologies 5500 Scanning Probe Microscope (PicoPlus-Atomic Force Microscopy Series 5500).

Box-counting method which uses Image J

Based on the assumption of the power law, distribution of pore sizes is only an approximation; a convenient way to evaluate the permeability-porosity is to utilize the geometric fractals as generating sets of the tube bundle cross section. This study will employ the box-counting method of fractal dimensions to analyze the membranes images obtained from SEM. The box-counting method covers the object being analyzed with tiles having the same dimensionality as the containing space. Since images are two-dimensional, the image is covered with squares of a certain size using the minimum number of squares to just completely cover the image of the object. Then, the process is repeated with smaller squares. The determination of the pore area fractal dimension was obtained by the box-counting method using Image J. By default, the box sizes in the table for counting the fractal (box) dimensions using ImageJ software are 2, 3, 4, 6, 8, 12, 16, 32, 64. FD measured by this technique is obtained from the slope of the double-logarithmic graph and is represented by Eq. 7.

$$\log N = FD \log \varepsilon, \tag{7}$$

where N is the number of full boxes, ε the length of one box, and FD is the 2D fractal dimension. There are two restrictions for the 2D-FD parameter of this technique. (1) The 2D-FD of a very dense cake the 2D-FD might be equal to 2 and in the presence of some porosity, 2D-FD value decreased between the range of 2 and 1. (2) The second limit concerns the necessity to have homogeneous surfaces [32].

Results and discussion

X-ray diffraction analysis

XRD analysis was used to provide definite structural information regarding the chemical composition of the membranes in order to indentify the phases of the materials. From Fig. 2a, b, similar phases occur at (O C N) and the angles where these phases occur are not the same. Similar phases occur at (O C) and the angles where these phases occur are not the same. Figure 2a shows that NF90-2540 consists of a pronounced diamond at the angle of 45 °C which is allotropes of carbon and one of the properties of diamond is high porosity. Karan et al. [33] demonstrated the ultrafast permeation of organic solvents through diamond-like carbon (DLC) nanosheets, freestanding amorphous carbon membranes: the membrane has a relatively porous layer of thickness $\sim$10 nm. In addition to their high permeability for various solvents, the membranes have excellent separation performance for organic solutes.

Scanning electron microscopy and Image J software

Surface morphology is very important in analyzing the performance in membrane technology. It provides a

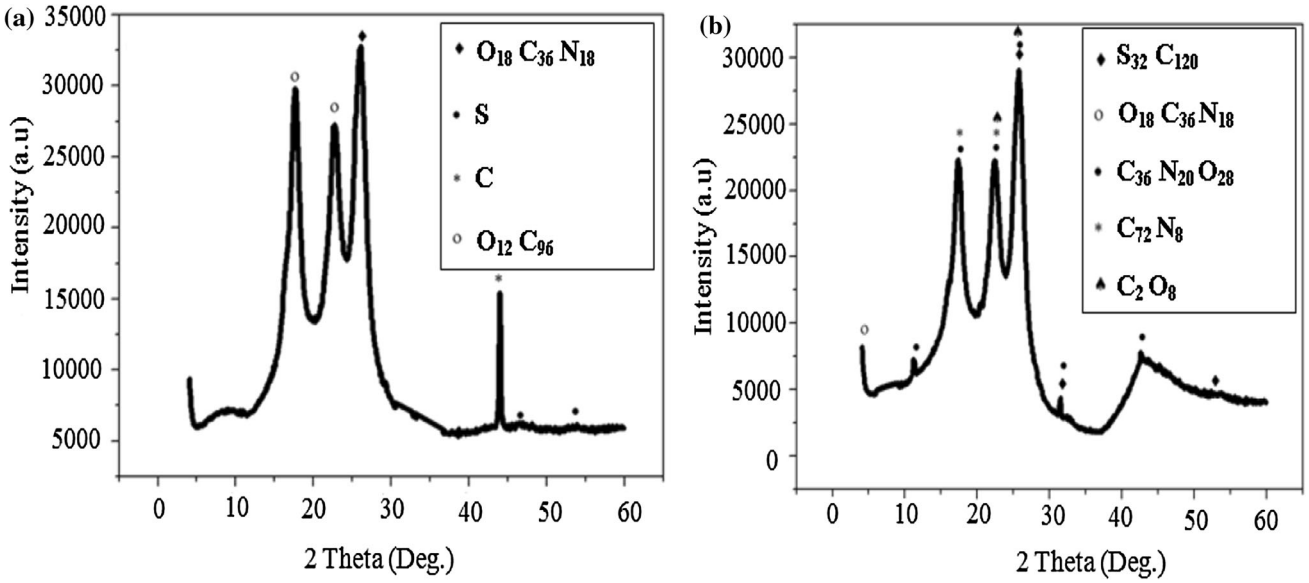

Fig. 2 X-ray diffraction of **a** NF90-2540, **b** NF1540-3

quantitative description of the structure of the membrane and the range of pore sizes present in a given membrane. It further gives more accurate description of the particle sizes that is likely to be retained by the membrane. With SEM, it was possible to observe the membrane skin layers and the inter-pore spacing. The surface structure of the nanofiltration membranes is shown in Fig. 3. NF1540-3 membrane appears relatively smooth with few visible pores, while NF90-2540 shows intertwined fibrous network with numerous pores. The threshold images were obtained from the SEM images using Image J software and the percentage porosity of NF90-2540 and NF1540-3 was found to be 27.42 and 14.14 %, respectively (see Fig. 4). The higher percentage porosity of NF90-2540 was as a result of the pronounced diamond at the angle of 45 °C which was observed in the XRD analysis.

Surface roughness determination

The surface roughness of the membranes surface was measured by a non-contact mode AFM. The surface roughness is important in evaluating the performance of a membrane because it could influence the transmembrane transport and fouling potential [34]. Some investigations have shown that surface roughness can be related to colloidal fouling, they further stated that surface roughness could also correlate with other material characteristics such as porosity and pore size distribution [35–37]. The image of NF90-2540 shows 3D orthographic structure with fine network-like fibrous structure with the occurrence of the tiny peaks and the valleys. NF1540-3 show fine network-like fibrous structure and higher ridges of 3D orthographic (see Fig. 5). The tiny peaks of NF90-

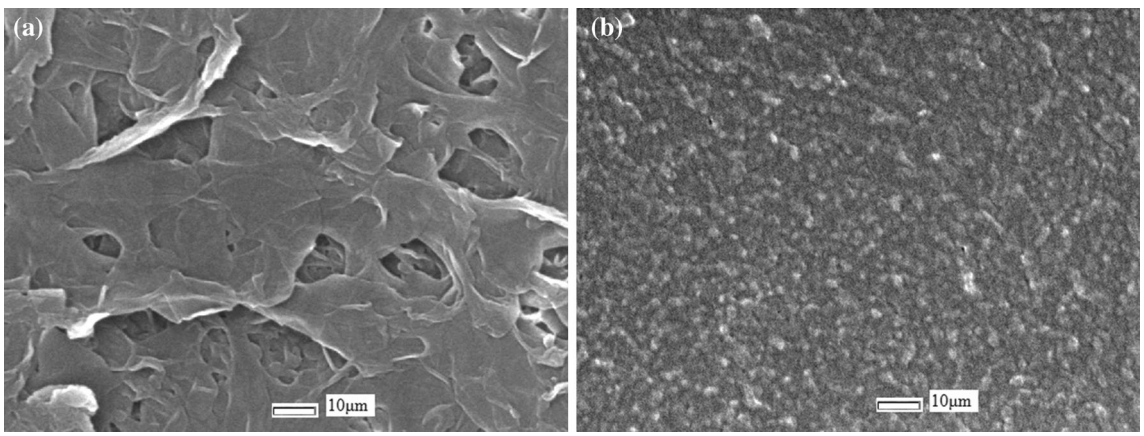

Fig. 3 SEM of **a** NF90-2540 **b** NF1540-3

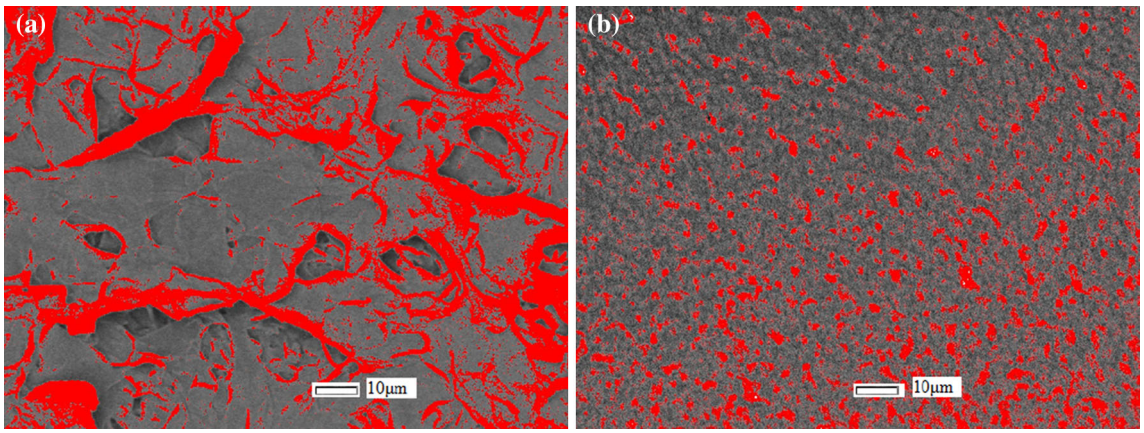

Fig. 4 Threshold image of **a** NF90-2540 **b** NF1540-3

2540 are responsible for the higher roughness of NF90-2540 compared with NF1540-3. The surface roughness of nanofiltration membranes can be attributed to a factor proportional to the bond strength of the membranes. The roughness parameter of the virgin NF90-2540 was 18.5; it was higher compared to the roughness parameter virgin NF1540-3 which was 0.079. The higher roughness leads to greater adhesive strength of the NF90-2540 and greater efficiency in the separation process [38]. The higher roughness of NF90-2540 was also as a result of the pronounced diamond at the angle of 45 °C which was observed in the XRD analysis.

Determination of 2D-FD from threshold image

The 2D fractal dimension parameter, denoted 2D-FD, was determined for the two nanofiltration membranes from scanning electronic microscopy (SEM) images applying the box-counting method on the threshold image (Fig. 4). 2D-FD of NF90-2540 is 1.9887 while the 2D-FD of NF1540-3 is 1.9511, as shown in Fig. 6a, b, respectively. The 2D-FD value for the NF90-2540 shows higher fractal dimension as a result of more porous surface which confirmed the presence of diamond observed in Fig. 2a. This also resulted to the high % porosity observed in Fig. 4a. The 2D-FD value for the NF1540-3 shows less porous surface which confirmed the low % porosity observed in Fig. 4b. Meng et al. [20, 26] employed fractal dimension analysis to analyze the cake layer formed in membrane bioreactors. These authors discovered that a lower value of fractal dimension corresponds to a lower value of porosity which was also coherent with trend observed in these results. The fractal dimension in NF1540-3 is related to the low % porosity and the less surface roughness observed with this membrane. The results in Fig. 6a, b can also be compared with theoretical model for fractal permeability developed by Yu and Cheng [39]. Figure 6a, b can be considered as the logarithmic plots of the cumulative number of macro-pores versus pore sizes $N(L \geq \lambda) \sim \lambda$ for the two bi-dispersed porous samples [39]. It can be seen that the number of cumulative macro-pores decreases as the pore size increases. The data follow a linear

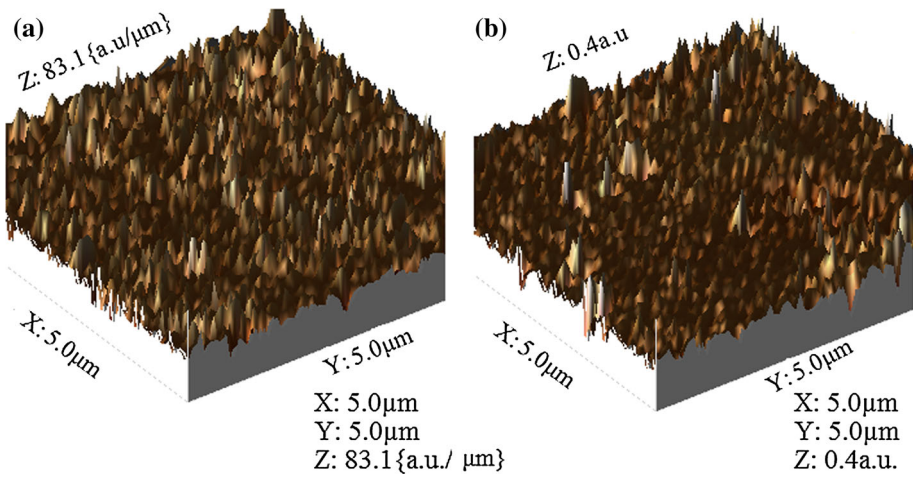

Fig. 5 Surface roughness of **a** NF 90-2540, **b** NF 1540-3

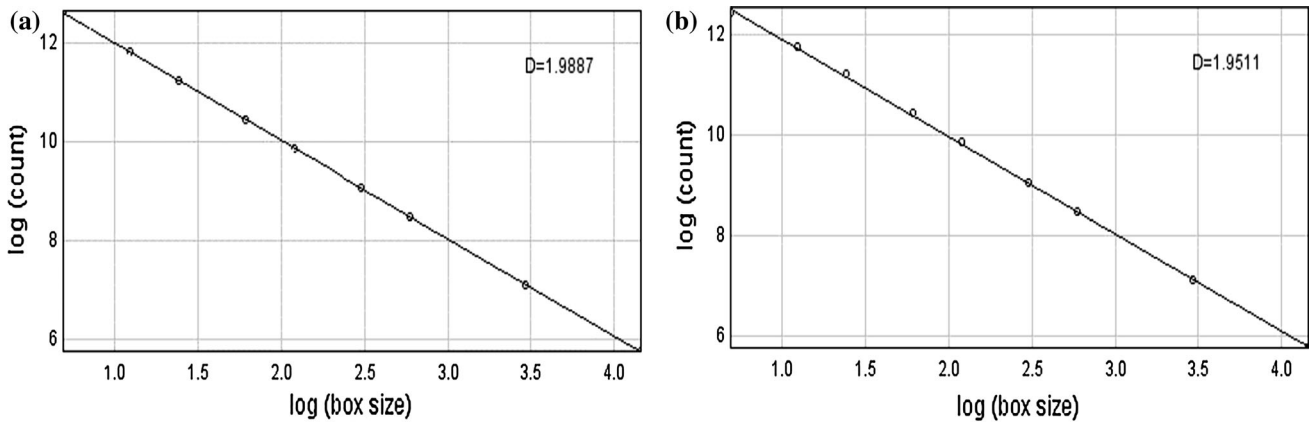

Fig. 6 Fractal dimension of **a** NF90-2540, **b** NF1540-3

relationship on the logarithmic scale, and this justified the statistical fractal nature of the microstructures of the bi-dispersed porous media. From the slopes of these straight lines the fractal dimensions were determined as 1.9887 for NF90-2540 and 1.9511 for NF1540-3.

Membrane permeability

Membrane permeability was observed for the synthetic solution of manganese and magnesium. The temperature of the flux was corrected by temperature correcting factor. Figure 7 shows the evolution of normalized flux with filtration time and filtered volume during constant pressure filtration of metal ions. In dead-end filtration, the rejected particles build up with time one the membrane surface or within the membrane. In either case, the particle builds due to an increased resistance to filtration and causes the permeate flux to decline. The permeate flux at different pH decreases with time as a function of the resistance caused both by fouling and concentration polarization/gel layer formation. It was observed that the permeate flux declined with time at the three different pH. Higher permeate flux was experienced at higher pH value (see Fig. 7); lower permeate flux at low pH values may be caused by many factors: (1) pore dimensions are controlled by pH and temperature. (2) Higher pH value may result in the increase in osmotic pressure at the solution membrane interface. (3) At low pH values, boundary layers at the membrane surface with higher hydraulic resistance are formed thereby reducing the permeate flux [40, 41]. Again, the sizes of the metal ions may strongly affect the transport mechanisms in membrane filtration systems. If metal ions have comparable or smaller sizes than the membrane pores, pore blocking may occur. It was described in Fig. 8 that the deposition of manganese and magnesium particles formed a monolayer at pH 2 which further inhibits additional particle deposition at pH 3 and pH 4, thereby blocking the surface of the membranes. Deposition processes were triggered by chemical conditions of the solution and favorable particle–surface interactions. The permeate flux can be related to the total hydraulic resistance by Darcy law given by Eq. 8:

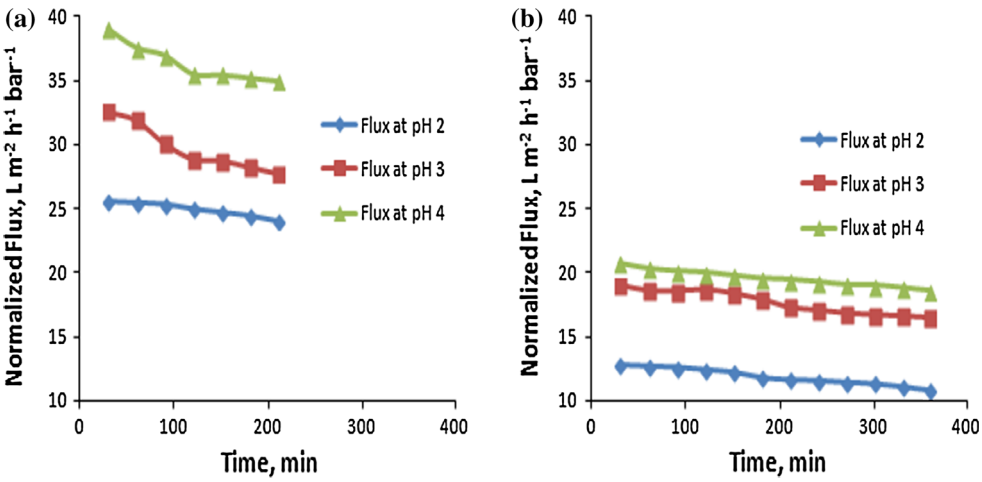

Fig. 7 Normalized flux as a function of time **a** NF90-2540, **b** NF1540-3 ($\Delta P = 10$ bars, $T = 25$ °C)

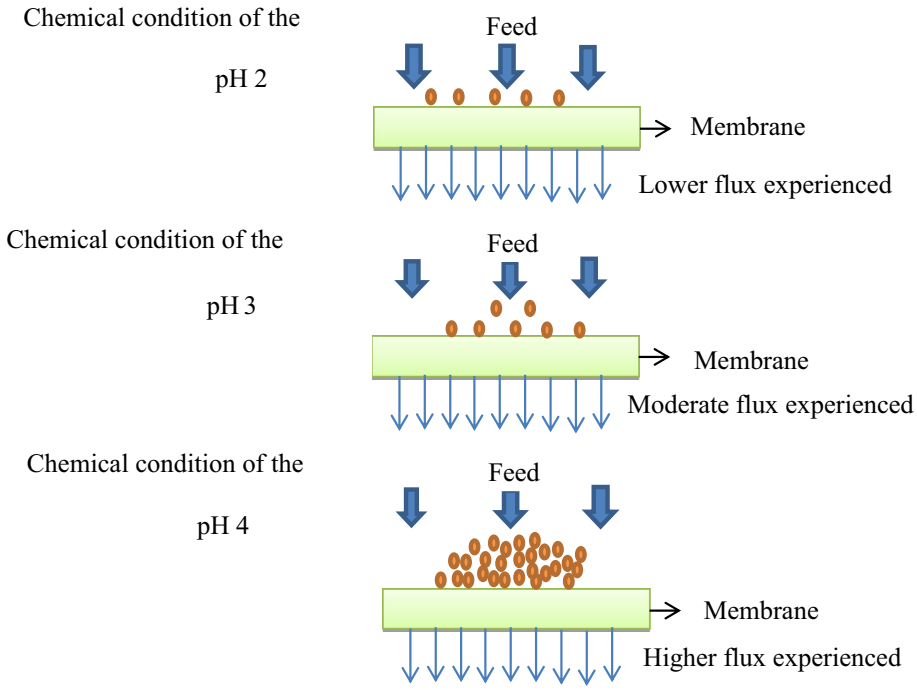

Fig. 8 Schematic description of the effect of pH in solution on the membrane surfaces; Initially, attached particles served as seeds for further particle deposition, which leads to the formation of thicker particle deposits

$$J_v = \frac{dv}{dt} = \frac{\Delta P}{\mu(R_m + R_c)}, \quad (8)$$

where R_m is membrane resistance ($1/m$), R_c is the resistance due to the cake layer, μ is the viscosity of the solution (cp), J_v is the flux (L m^{-2} h^{-1}), ΔP is the transmembrane pressure (bar).

The permeate flux in Eq. 6 does not take into account the total hydraulic resistance and Darcy law. The Eq. 6 was used to find the normalized flux after filtration experiments at different pH values. The permeate flux in Eq. 8 took into account total hydraulic resistance and Darcy law because the deposition processes was triggered by chemical conditions (addition of NaOH to the salts in order to increase the pH values) of the solution and the favorable particle–surface interactions.

Influence of pH on pores and fractal dimension

In order to analyze the microstructure of the ion deposition, 2D measurement of the fractal dimension (2D-FD) was done on the surface deposited with ions at different pH values. The fractal dimension of the fouled membranes was determined from SEM images (see Figs. 9, 10) using the box-counting method. The 2D-FD values of NF1540-3 membrane after experiments at pH 2, pH 3, and pH 4 are 1.9289, 1.8925, and 1.7742, respectively (see Fig. 11). While the 2D-FD values of NF90-2540 membrane after experiments at pH 2, pH 3, and pH 4 are 1.9835, 1.8579, and 1.5731, respectively (see Fig. 12). The fractal dimension of the used membranes was observed in Figs. 11 and 12. The value of fractal dimension observed for the particle deposited at pH 4 was 1.7742 and 1.5431 for NF1540-3 and NF90-2540, respectively, and a higher value of 2D-FD (1.9289 and 1.9835 for NF1540-3 and NF90-2540, respectively) was found for particle deposited at pH 2. Furthermore, fractal dimension observed for the particle deposited at pH 3 was 1.8925 and 1.8579 for NF 1540-3 and NF90-2540, respectively, which indicated that more particles were deposited at pH 4 (see Fig. 8). One can see that the higher the pH, the lower the fractal dimension of the membranes due to the blockage of pores. A higher value of fractal dimension indicates a lower value of permeability in the fouled state (or a dense and compact cake layer) [32]. The role of pH on the fractal dimension of the membranes after the exposure of the membranes to the solution was investigated. It was observed that 2D-FD parameters of fouled membranes were in a decreasing trend with increasing pH, in other words, fractal dimension increased with the decrease in permeability, as shown in Fig. 13. It can be correlated from the values obtained from fractal dimension that a higher value of fractal dimension corresponds to a lower value of permeability. Similar trends were observed in the literature; Meng et al. [26] investigated the fouling of membrane bioreactor due to cake formation using fractal theory [26, 41]. They observed that fractal dimension has a linear relationship with cake porosity. According to their observations, permeability increased as FD decreased which was also observed in this investigation. Pontié et al. [32] also observed the same trend in their investigation of clay filter-aid in ultrafiltration (UF) of humic acid solution.

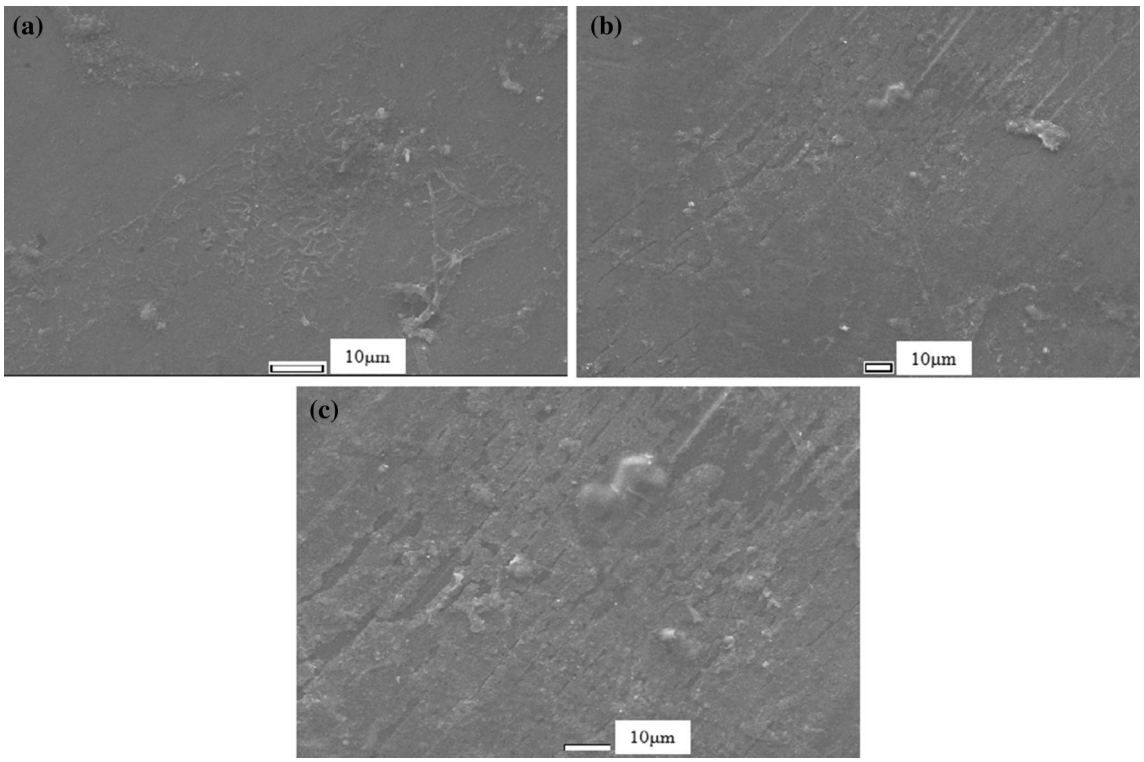

Fig. 9 SEM images showing the membrane surfaces of NF1540-3 membrane fouled by synthetic solutions of manganese and magnesium ions at **a** pH 2, **b** pH 3, and **c** pH 4

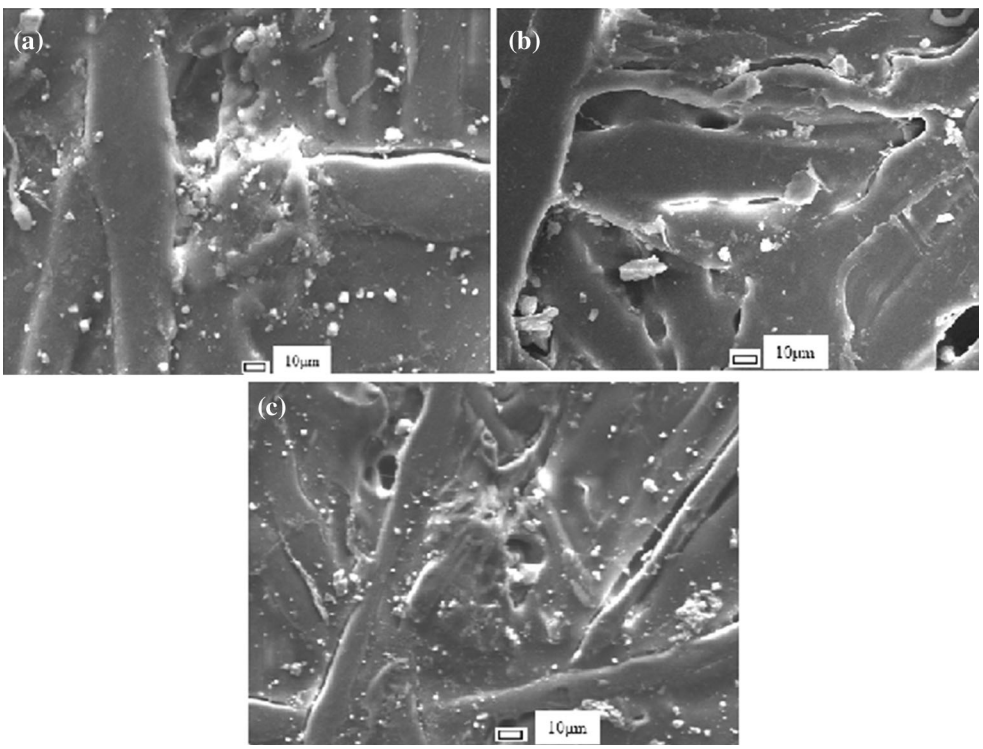

Fig. 10 SEM images showing the membrane surfaces of NF90-2540 membrane fouled by synthetic solutions of manganese and magnesium ions at **a** pH 2, **b** pH 3, and **c** pH 4

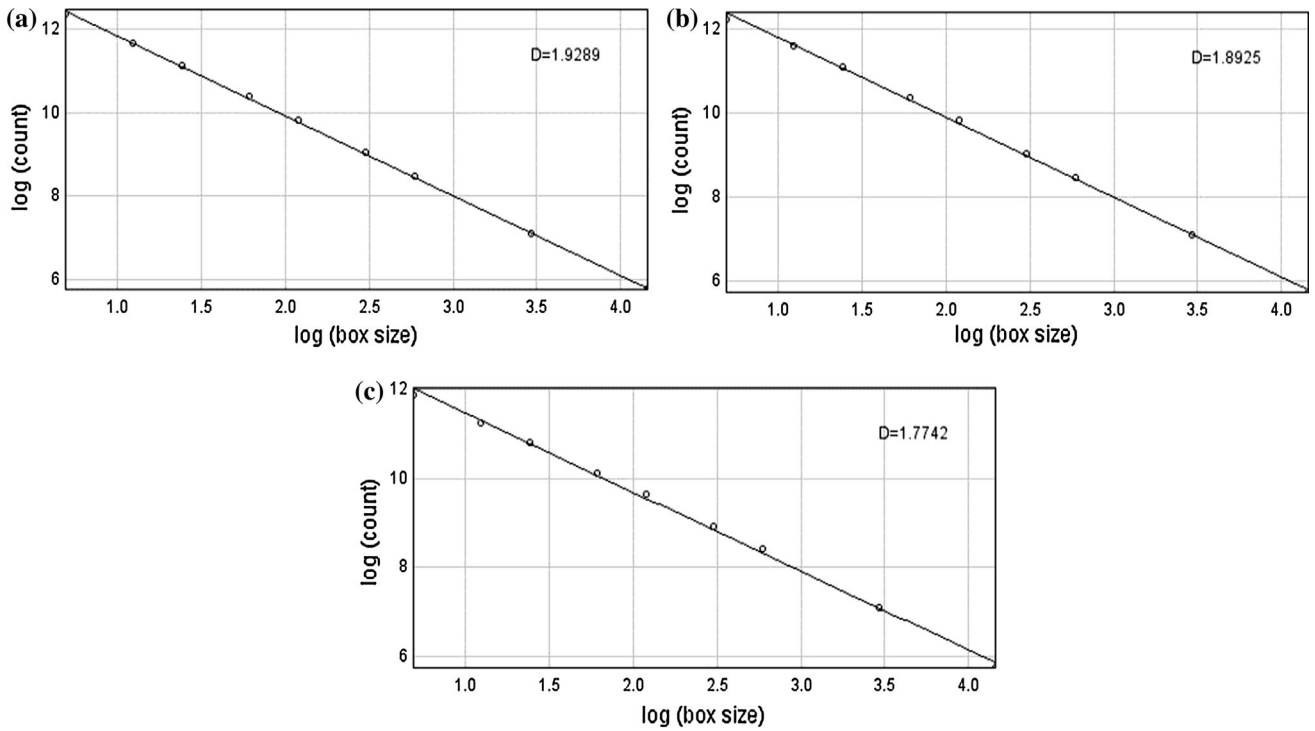

Fig. 11 Fractal dimension of NF1540-3 after filtration at **a** pH 2, **b** pH 3, **c** pH 4

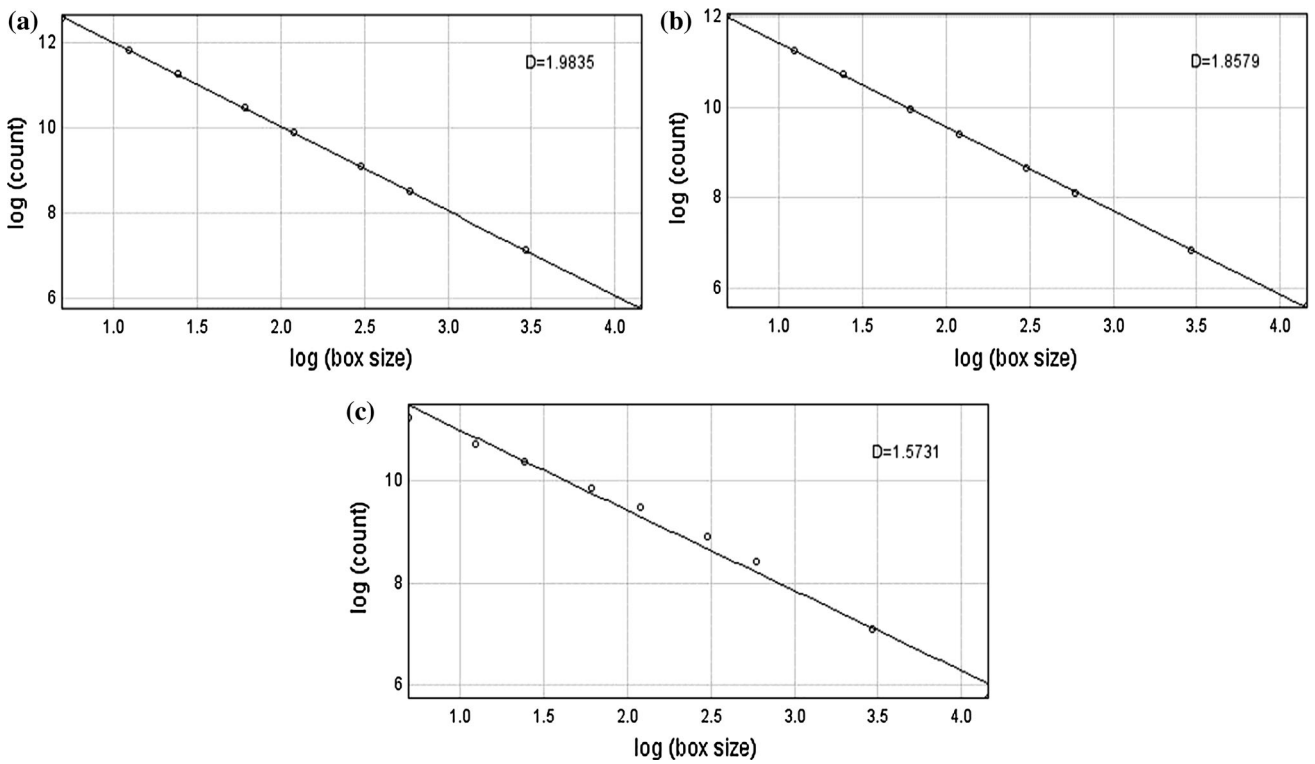

Fig. 12 Fractal dimension of NF90-2540 after filtration at **a** pH 2, **b** pH 3, **c** pH 4

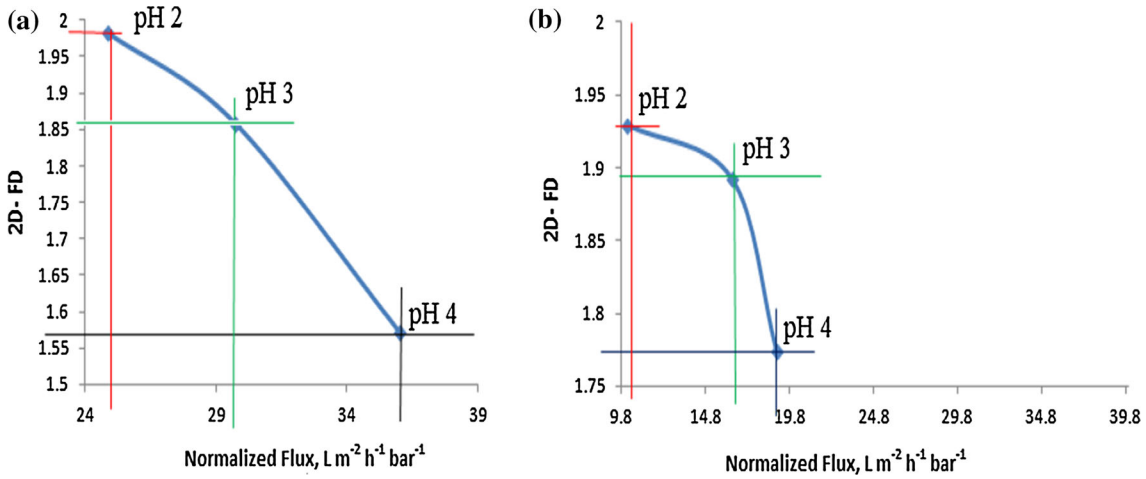

Fig. 13 Evolution of fractal dimension values with **a** NF90-2540 **b** NF 1540-3 after filtration at pH 2, pH 3, and pH 4 ($\Delta P = 10$ bars, $T = 25$ °C)

Rejection of ions

The influence of pH on salt rejections of the ions was investigated in Fig. 14; the salt rejection was higher at higher pH values for the two metal ions result in the increase in osmotic pressure at the solution–membrane interface. An explanation for comparing the rejection sequence of these cations can be found by comparing the diffusion coefficients of the different cations [42]. The diffusion coefficient of Mn^{2+} and Mg^{2+} in water at 25 °C are 1.424×10^{-5} cm^2 s^{-1}, 1.412×10^{-5} cm^2 s^{-1}, respectively [43]. It was assumed that the diffusion coefficients in a membrane can be approximated by those in aqueous solutions. The order of diffusion coefficients is inversely reflected in the rejection sequence, so that diffusion seems to be an important transport mechanism [40].

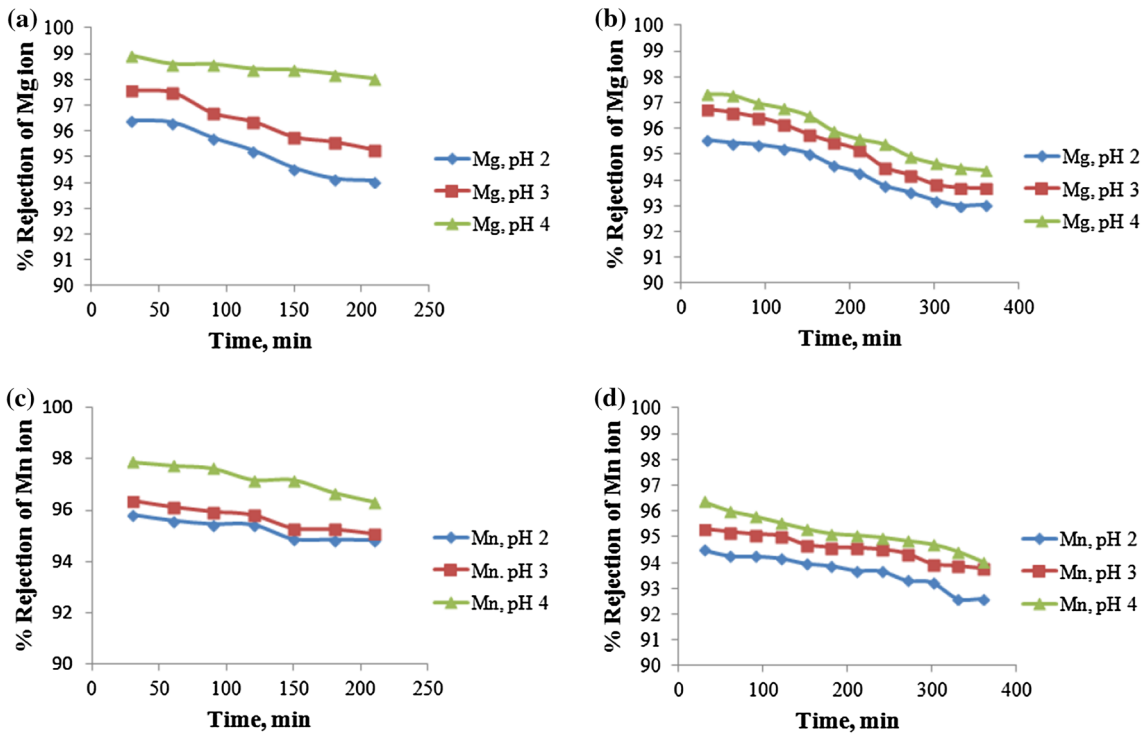

Fig. 14 % rejection of ions as a function of time **a** Mg ions rejected by NF90-2540; **b** Mg ions rejected by NF1540-3; **c** Mn ions rejected by NF90-2540 **d** Mn ions rejected by NF1540-3 ($\Delta P = 10$ bars, $T = 25$ °C)

A high diffusion coefficient of Mn^{2+} resulted in a lower rejection of Mn^{2+} for the three pH values by the membranes. Similar trends were observed in the literature [42, 44]. The rejection behavior of the metal ions at different pH values can also be correlated to the values obtained from fractal dimension; that a higher value of fractal dimension of the used membrane at a lower pH corresponds to a lower rejection of the metal ions. Agboola et al. [45] have demonstrated that the difference in the rejection rate is caused by the membrane structure, which depends on the pH.

Conclusion

The theory of the fractal analysis done by a box-counting method was used to describe the porosity of the membranes. The 2D-FD parameters of fouled membranes were in a decreasing trend with increasing pH, therefore, the fractal dimension increased with the decrease in permeability. It was correlated from the values obtained from fractal dimension that a higher value of fractal dimension corresponds to a lower value of permeability. The rate of flux decline depends on pore size and fractal dimension; A higher value of fractal dimension of the used membranes indicates a lower value of permeability in the fouled state. It was further used to correlate the rejection behavior of the metals at different pH values. Results obtained showed that that a higher value of fractal dimension of the used membrane at a lower pH corresponds to a lower rejection of the metal ions.

References

1. Yu BM (2005) Fractal character for tortuous stream tubes in porous media. Chin Phys Lett 22(1):158–160
2. Al-Mossawy MI, Demiral B, Raja DMA (2011) Foam dynamics in porous media and its applications in enhanced oil recovery: review. IJRRAS 7(4):351–359
3. Howell JR, Hall MJ, Ellzey JL (1996) Combustion of hydrocarbon fuels within porous inert media. Prog Energy Combust Sci 122:121–145. doi:10.1016/0360-1285(96)00001-9
4. Kamal MM, Mohamad AA (2006) Combustion in porous media: a review. J Power Energy 220:487–508. doi:10.1243/09576509JPE169
5. Wood S, Harris AT (2008) Porous burners for lean-burn applications. Prog Energy Combust Sci 34:667–684. doi:10.1016/j.pecs.2008.04.003
6. Bowles J (1984) Physical and geotechnical properties of soil, 2nd edn. McGraw-Hill Book Company, New York
7. Shkolnikov V, Strickland DG, Fenning DP, Santiago JG (2010) Design and fabrication of porous polymer wick structures. Sens Actuators B 150:556–563. doi:10.1016/j.snb.2010.08.040
8. Cuperus FP, Smolders CA (1991) Characterization of UF membranes: membrane characteristics and characterization techniques. Adv Colloid Interface Sci 34:135–173. doi:10.1016/0001-8686(91)80049-P
9. Helwani Z, Wiheeb AD, Shamsudin IK, Kim J, Othman MR (2015) The effects of fractality on hydrogen permeability across meso-porous membrane. Heat Mass Transfer 51:751–758. doi:10.1007/s00231-014-1445-7
10. Burggraaf AJ, Cot L (1996) Fundamentals of inorganic membranes science and technology, vol 4. Elsevier, Amsterdam
11. Kikkinides ES, Stoitsas KA, Zaspalis VT, Burganos VN (2004) Simulation of structural and permeation properties of multi-layer ceramic membranes. J Membr Sci 243:133–149. doi:10.1016/j.memsci.2004.06.019
12. Mandelbrot BB (1982) The fractal geometry of nature. Freeman, New York, p 23
13. Pitchumani R, Ramakrishnan BA (1999) Fractal geometry model for evaluating permeabilities of porous performs used in liquid composite molding. Int J Heat Mass Transfer 42:2219–2232
14. Zhang L-Z (2008) A fractal model for gas permeation through porous membranes. Int J Heat Mass Transfer 51:5288–5295. doi:10.1016/j.ijheatmasstransfer.2008.03.008
15. Ibaseta N, Biscans B (2010) Fractal dimension of fumed silica: comparison of light scattering and electron microscope methods. Powder Technol 203:206–210. doi:10.1016/j.poetec.2010.05.010
16. Yu BM (2001) Comments on a fractal geometry model for evaluating permeabilities of porous preforms used in liquid composite molding. Int J Heat Mass Transfer 44:2787–2789
17. Gmachowski L (2003) Transport properties of fractal aggregates calculated by permeability. Colloids Surf A 215:173–179. doi:10.1016/S0927-7757(02)00440-5
18. Gmachowski L (2003) Mass- radius relation for fractal aggregates of polydisperse particles. Colloids Surf A 224:45–52. doi:10.1016/S0927-7757(03)00318-2
19. Mandelbrot BB (1977) Fractal-form: chance and dimension, vol 1. Freeman, San Francisco
20. Meng FG, Zhang HM, Li YS, Zhang XW, Yang FL, Xiao JN (2005) Cake layer morphology in microfiltration of activated sludge wastewater based on fractal analysis. Sep Purif Technol 44:250–257. doi:10.1016/j.seppur.2005.01.015
21. Cai J, Perfect E, Cheng C-L, Hu X (2014) Generalized modeling of spontaneous imbibition based on Hagen-Poiseuille flow in tortuous capillaries with variably shaped apertures. Langmuir 30:5142–5151. doi:10.1021/la5007204
22. Kaye BH (1991) Characterizing the structure of fumed pigments using the concepts of fractal geometry. Part Part Syst Charact 9:63–71. doi:10.1002/ppsc.19910080112
23. Kaye BH (1993) Applied fractal geometry and the fineparticle specialist. Part I: Rugged boundaries and rough surfaces. Part Part Syst Charact 10:99–110. doi:10.1002/ppsc.19930100302
24. Xu L, Zhu QX, Lu SQ (2000) Study on the cake structure of cross-flow micro-filtration. In: Proceedings the 8th World filtration Congress, London, p 449
25. Syvitski JPM (2007) Principle, methods and applications of particle size analysis. Cambridge University Press, New York, p 99
26. Meng F, Zhang H, Li Y, Zhang Z, Yang F (2005) Application of fractal permeation model to investigate membrane fouling in membrane bioreactor. J Membr Sci 262:107–116. doi:10.1016/j.memsci.2005.04.013
27. Akbari A, Homayonfal M, Jabbari V (2010) Synthesis and characterization of composite polysulfonemembranes for desalination in nanofiltration technique. Water Sci Technol 62(11):2655–2663. doi:10.2166/wst.2010.512
28. Alayemieka E, Lee S (2013) Modification of polyamide membrane surface with chlorine dioxide solutions of differing pH. Desalin Water Treat 45:84–90

29. Said MM, El-Aassar AHM, Kotp YH, Shawky HA, Abdel Mottaleb MSA (2013) Performance assessment of prepared polyamide thin film composite membrane for desalination of saline groundwater at Mersa Alam-Ras Banas, Red Sea Coast, Egypt. Desalin Water Treat 51:4927–4937. doi:10.1080/19443994.2012.692013
30. Omidvar M, Mousavi SM, Soltanieh M, Safekordi AA (2014) Preparation and characterization of poly (ethersulfone) nanofiltration membranes for amoxicillin removal from contaminated water. J Environ Sci Eng 12(18):1–9. doi:10.1186/2052-336X-12-18
31. Horcas I, Fernandez R, Gomez-Rodriguez JM, Colchero J, Gomez-Herrero J, Baro AM (2007) WSXM: software for scanning probe microscopy and tool for nanotechnology. Rev Sci Instrum 78:013705–013708. doi:10.1063/1.2432410
32. Pontié M, Thekkedath A, Kecili K, Dach H, De Nardi F, Castaing JB (2012) Clay filter-aid in ultrafiltration (UF) of humic acid solution. Desalin 292:73–86. doi:10.1016/j.desal.2012.02.011
33. Karan S, Samitsu S, Peng X, Kurashime K, Ichinose I (2012) Ultrafast viscous permeation of organic solvents through diamond-like carbon nanosheets. Science 335:444–447. doi:10.1126/science.1212101
34. Khulbe KC, Feng CY, Matsuura TS (2008) Synthetic polymeric membranes characterization by atomic force microscopy, vol 2. Springer, Berlin
35. Song L, Johnson PR, Elimelech M (1994) Kinetics of colloid deposition onto heterogeneously charged surfaces in porous media. Environ Sci Technol 28:1164–1171. doi:10.1021/es00055a030
36. Vrijenhoek EM, Hong S, Elimelech M (2001) Influence of membrane surface properties on initial rate of colloidal fouling of reverse osmosis and nanofiltration membranes. J Membr Sci 188:115–128. doi:10.1016/S0375-7688(01)00376-3
37. Bowen WR, Doneva TA (2000) Atomic force microscopy studies of membranes: effect of surface roughness on double layer interaction and particle adhesion. J Colloid Interface Sci 229(2):544–549. doi:10.1016/jcis.2000.6997
38. Bowen WR, Hilal N, Lovitt RW, Wright CJ (1998) A new technique for membrane characterization: direct measurement of the force of adhesion of a single particle using atomic force microscopic. J Membr Sci 139(2):269–274
39. Yu B, Cheng P (2002) A fractal permeability model for bi-dispersed porous media. Int J Heat Mass Transfer 45:2983–2993
40. Alpatova A, Verbych S, Bryk M, Nigmatullin R, Hilal N (2004) Ultrafiltration of water containing natural organic matter: heavy metal removing in the hybrid complexation-ultrafiltration process. Sep Purif Technol 40(2):155–162. doi:10.1016/j.seppur.2004.02.003
41. Lin Y-L (2013) Effect of physiochemical properties of nanofiltration membranes on the rejection of small organic DBP precursors. J Environ Eng 139:127–136. doi:10.1061/(ASCE)EE.1943-7870.0000623
42. Chaudhari LB, Murthy ZVP (2008) Removal of nickel and cadmium ions from aqueous waste by a nanofiltration. J Environ Res Dev 3:400–406
43. Vanysek P (2005) Ionic conductivity and diffusion at infinite dilution in: CRC handbook of chemistry and physics, vol 5, 90th edn. CRC Press, Boca Raton
44. Mohammad AW, Othaman R, Hilal N (2004) Potential use of nanofiltration membranes in treatment of industrial wastewater from Ni-P electroless plating. Desalin 168:241–252. doi:10.1016/j.desal.2004.07.004
45. Agboola O, Maree J, Mbaya R, Kolesnikov A, Sadiku R, Verliefde A, D'Haes A (2015) Microscopical characterization of nanofiltration membranes for the removal of nickel ions from aqueous solution. Korean J Chem Eng 32(4):731–742. doi:10.1007/s11814-014-0290-1